Supplementary Materials for

Planar photonic chips with tailored dispersion relations for high-efficient spectrographic devices

Yikai Chen[1], Zetao Fan[2], Wenjie Sun[1], Zekai Wang[1], Xueqin Wu[1], Jiale Zheng[1], Junfeng Li[1], Shijun Zhu[1] and Douguo Zhang[2*]

[1]School of Sciences, Nanjing University of Science and Technology, Nanjing 210094, China

[2]Advanced Laser Technology Laboratory of Anhui Province, Department of Optics and Optical engineering, University of Science and Technology of China, Hefei, Anhui 230026, China

[*]Corresponding author: dgzhang@ustc.edu.cn

Note 1. The principle of reconstructing the spectra from the reflection images.

Retrieving unknown spectrum from the experimental or calculated results is a process to solve an inverse problem, which can be represented by the following matrix equation $RI_{\lambda} = I_{\theta}$, that is

$$\begin{pmatrix} R_{\lambda1,\theta1}, R_{\lambda2,\theta1}, R_{\lambda3,\theta1}, \cdots, R_{\lambda m,\theta1} \\ R_{\lambda1,\theta2}, R_{\lambda2,\theta2}, R_{\lambda3,\theta2}, \cdots, R_{\lambda m,\theta2} \\ R_{\lambda1,\theta3}, R_{\lambda2,\theta3}, R_{\lambda3,\theta3}, \cdots, R_{\lambda m,\theta3} \\ \vdots \\ R_{\lambda1,\theta n}, R_{\lambda2,\theta n}, R_{\lambda3,\theta n}, \cdots, R_{\lambda m,\theta n} \end{pmatrix} \begin{pmatrix} I_{\lambda1} \\ I_{\lambda2} \\ I_{\lambda3} \\ \vdots \\ I_{\lambda n} \end{pmatrix} = \begin{pmatrix} I_{\theta1} \\ I_{\theta2} \\ I_{\theta3} \\ \vdots \\ I_{\theta m} \end{pmatrix} \qquad \text{(S1)}$$

Here, R is the coefficient matrix for the spectral-retrieving, where each element ($R_{\lambda i,\theta i}$) of this matrix corresponds to the reflectance at a certain wavelength and a certain angle. $I_{\lambda i}$ is spectral intensity matrix (incident intensity of the light source at the wavelength λ_i), representing the spectral of the light source (unknown and to be derived). $I_{\theta i}$ is the reflection intensity matrix, each element ($I_{\theta i}$) represents intensity of the reflected light at angle θ_i (it can be measured with the detector, such as the camera).

To determine the matrix R, the reflection intensity is measured when a monochromatic light with a unit intensity is incident on the system. From $RI_{\lambda i} = I_{\theta}(\lambda)$, we can get $R(\lambda) = I_{\theta}(\lambda) I_{\lambda i}^{-1}$, then Eq (S1) can be simplified as Eq. (S2)

$$\begin{pmatrix} R_{\lambda1,\theta1}, R_{\lambda2,\theta1}, \cdots R_{\lambda i,\theta1}, \cdots, R_{\lambda m,\theta1} \\ R_{\lambda1,\theta2}, R_{\lambda2,\theta2}, \cdots R_{\lambda i,\theta2}, \cdots, R_{\lambda m,\theta2} \\ R_{\lambda1,\theta3}, R_{\lambda2,\theta3}, \cdots R_{\lambda i,\theta3}, \cdots, R_{\lambda m,\theta3} \\ \vdots \\ R_{\lambda1,\theta n}, R_{\lambda2,\theta n}, \cdots R_{\lambda i,\theta n}, \cdots, R_{\lambda m,\theta n} \end{pmatrix} \begin{pmatrix} 0 \\ \vdots \\ I_{\lambda i} \\ \vdots \\ 0 \end{pmatrix} = \begin{pmatrix} I_{\theta1} \\ I_{\theta2} \\ I_{\theta3} \\ \vdots \\ I_{\theta m} \end{pmatrix} \rightarrow \begin{pmatrix} \cdots R_{\lambda i,\theta1}, \cdots \\ \cdots R_{\lambda i,\theta2}, \cdots \\ \cdots R_{\lambda i,\theta3}, \cdots \\ \vdots \\ \cdots R_{\lambda i,\theta n}, \cdots \end{pmatrix} = \begin{pmatrix} I_{\theta1} \\ I_{\theta2} \\ I_{\theta3} \\ \vdots \\ I_{\theta m} \end{pmatrix} \begin{pmatrix} 0 \\ \vdots \\ I_{\lambda i} \\ \vdots \\ 0 \end{pmatrix}^{-1} \qquad \text{(S2)}$$

The full range of coefficients can be obtained by traversing all the wavelengths. It depends only on the structural parameters of the system. Therefore, the spectral intensity matrix (the spectrum to be retrieved) can be obtained from the reflectance intensity and the coefficient matrix.

$$I_{\lambda} = R^{-1} I_{\theta} \quad \text{(S3)}$$

But if there is any detection noise (then, $RI_{\lambda} = I_{\theta} + I_{noise}$), even the noise is very weak ($I_{noise} << I_{\theta}$), it will bring huge errors in solving the matrix equation. Therefore, various algorithms are proposed to optimize the solutions[1, 2, 3]. Different from these conventional means of applying the inversion algorithm, in this work, we design the suitable structures to construct a special matrix, which can simplify the process to solve the matrix equation and then retrieve the accurate spectrum. This special matrix ca be the diagonal matrix, etc.

For examples, if

$$R = \begin{pmatrix} R_{\lambda 1,\theta 1}, 0, 0, \cdots, 0 \\ 0, R_{\lambda 2,\theta 2}, 0, \cdots, 0 \\ 0, 0, R_{\lambda 3,\theta 3}, \cdots, 0 \\ \vdots \\ 0, 0, 0, \cdots, R_{\lambda m,\theta n} \end{pmatrix} \quad \text{(S4)}$$

and $R_{\lambda 1,\theta 1}, R_{\lambda 2,\theta 2}, R_{\lambda 3,\theta 3}, \cdots, R_{\lambda m,\theta n} = 1$, then the matrix equation can be simplified as Eq. (S5)

$$\begin{pmatrix} I_{\lambda 1} \\ I_{\lambda 2} \\ I_{\lambda 3} \\ \vdots \\ I_{\lambda n} \end{pmatrix} = \begin{pmatrix} I_{\theta 1} \\ I_{\theta 2} \\ I_{\theta 3} \\ \vdots \\ I_{\theta m} \end{pmatrix} \quad \text{(S5)}$$

It means that the spectrum can be derived without the matrix solving process (avoiding noise interference). If the elements $R_{\lambda m,\theta n}$ are not equal to 1, it is equivalent to dividing the intensity at each the corresponding angle by a factor to obtain the spectrum.

Taking advantages of the low-loss BSW modes sustained on an all-dielectric multilayer structure, this special matrix can be constructed as Eq. (S6).

$$R = \begin{pmatrix} R_r, \cdots, R_{\lambda 1,\theta 1}, R_r, R_r, \cdots R_r, \cdots, R_r \\ R_r, \cdots, R_r, R_{\lambda 2,\theta 2}, R_r, \cdots R_r, \cdots, R_r \\ R_r, \cdots, R_r, R_r, R_{\lambda 3,\theta 3}, \cdots R_r, \cdots, R_r \\ \vdots \\ R_r, \cdots, R_r, R_r, R_r, \cdots R_{\lambda n,\theta n}, \cdots, R_r \end{pmatrix} \tag{S6}$$

It has two characteristics. Firstly, the diagonal matrix elements $R_{\lambda i,\theta i}$ are of extremely small values (meaning that the reflectance at the excitation angle and excitation wavelength of the BSWs is very small). The value of other elements (R_r) are close to 1 (meaning the reflectance in the case of attenuated total reflection). Here the incident angle is ranged from 41° to 48° (in the region near the excitation angle of the BSWs mode on the designed multilayer-chip). Then, we have the following matrix as shown in Eq. (7).

$$R_{BSW} = \begin{pmatrix} R_r, \cdots, R_{\lambda 1,\theta 1}, R_r, R_r, \cdots R_r, \cdots, R_r \\ R_r, \cdots, R_r, R_{\lambda 2,\theta 2}, R_r, \cdots R_r, \cdots, R_r \\ R_r, \cdots, R_r, R_r, R_{\lambda 3,\theta 3}, \cdots R_r, \cdots, R_r \\ \vdots \\ R_r, \cdots, R_r, R_r, R_r, \cdots R_{\lambda n,\theta n}, \cdots, R_r \end{pmatrix} \tag{S7}$$

Therefore, for the spectra characterization process, from (1), $R_{BSW} I_\lambda = I_\theta$ can be written as Eq. (S8)

$$\begin{pmatrix} R_r, \cdots, R_{\lambda 1,\theta 1}, R_r, R_r, \cdots R_r, \cdots, R_r \\ R_r, \cdots, R_r, R_{\lambda 2,\theta 2}, R_r, \cdots R_r, \cdots, R_r \\ R_r, \cdots, R_r, R_r, R_{\lambda 3,\theta 3}, \cdots R_r, \cdots, R_r \\ \vdots \\ R_r, \cdots, R_r, R_r, R_r, \cdots R_{\lambda n,\theta n}, \cdots, R_r \end{pmatrix} \begin{pmatrix} \vdots \\ I_{\lambda 1} \\ I_{\lambda 1} \\ I_{\lambda 1} \\ \vdots \\ I_{\lambda n} \\ \vdots \end{pmatrix} = \begin{pmatrix} \vdots \\ I_{\theta 1} \\ I_{\theta 2} \\ I_{\theta 3} \\ \vdots \\ I_{\theta m} \\ \vdots \end{pmatrix} \tag{S8}$$

Secondly, if the top space of the dielectric multilayer is full of moisture, the BSWs cannot be excited at the top surface of the dielectric multilayer, then the R_r changes to $R_r^{'}$ but they are of nearly the same value. In this case, no BSWs are excited, and then the value of $R_{\lambda i,\theta i}$ is also close to 1. Then, in this case, the matrix equation can be written as ($R_{BSW-off} I_\lambda = I_\theta$) shown in Eq. (S9)

$$\begin{pmatrix} R_r^{'},\cdots,R_{\lambda1,\theta1}^{'},R_r^{'},R_r^{'},\cdots R_r^{'},\cdots,R_r^{'} \\ R_r^{'},\cdots,R_r^{'},R_{\lambda2,\theta2}^{'},R_r^{'},\cdots R_r^{'},\cdots,R_r^{'} \\ R_r^{'},\cdots,R_r^{'},R_r^{'},R_{\lambda3,\theta3}^{'},\cdots R_r^{'},\cdots,R_r^{'} \\ \vdots \\ R_r^{'},\cdots,R_r^{'},R_r^{'},R_r^{'},\cdots R_{\lambda n,\theta n}^{'},\cdots,R_r^{'} \end{pmatrix} \begin{pmatrix} \vdots \\ I_{\lambda1} \\ I_{\lambda1} \\ I_{\lambda1} \\ \vdots \\ I_{\lambda n} \\ \vdots \end{pmatrix} = \begin{pmatrix} \vdots \\ I_{\theta1} \\ I_{\theta2} \\ I_{\theta3} \\ \vdots \\ I_{\theta m} \\ \vdots \end{pmatrix} \quad \text{(S9)}$$

After differential processing for above two equations, we get Eq. (S10)

$$\begin{pmatrix} 0,\cdots,R_{\lambda1,\theta1}^{'}-R_{\lambda1,\theta1},0,0,\cdots 0,\cdots,0 \\ 0,\cdots,0,R_{\lambda2,\theta2}^{'}-R_{\lambda2,\theta2},0,\cdots 0,\cdots,0 \\ 0,\cdots,0,0,R_{\lambda3,\theta3}^{'}-R_{\lambda3,\theta3},\cdots 0,\cdots,0 \\ \vdots \\ 0,\cdots,0,0,0,\cdots R_{\lambda n,\theta n}^{'}-R_{\lambda n,\theta n},\cdots,0 \end{pmatrix} \begin{pmatrix} \vdots \\ I_{\lambda1} \\ I_{\lambda1} \\ I_{\lambda1} \\ \vdots \\ I_{\lambda n} \\ \vdots \end{pmatrix} = \begin{pmatrix} \vdots \\ I_{\theta1} \\ I_{\theta2} \\ I_{\theta3} \\ \vdots \\ I_{\theta m} \\ \vdots \end{pmatrix} \quad \text{(S10)}$$

Since $R_{\lambda1,\theta1},R_{\lambda2,\theta2},R_{\lambda3,\theta3},\cdots,R_{\lambda m,\theta n}$ are approximately of the same value in the constructed matrix, the matrix can be further simplified as following.

$$\begin{pmatrix} I_{\lambda1} \\ I_{\lambda1} \\ I_{\lambda1} \\ \vdots \\ I_{\lambda n} \end{pmatrix} = -C\cdot \begin{pmatrix} I_{\theta1} \\ I_{\theta2} \\ I_{\theta3} \\ \vdots \\ I_{\theta m} \end{pmatrix},$$ that is

$$I_{\lambda} = -CI_{\theta} \quad \text{(S11)}$$

Here, C is a constant that reflects the relationship between incident and reflected light. Since each corresponding element in the spectral intensity matrix (I_{λ}) and the reflection intensity matrix (I_{θ}) has the same relative intensity relationship. Therefore, the incident intensity of the light source at each wavelength is corresponding to the reflection intensity at the corresponding angle (or position of the camera image), then the spectrum of the light source can be derived out from the reflectance image.

Note 2. Determining the wavelength of the light point from its position on the reflectance image

Through the geometric structure of the optical elements used in the experimental set-up, the relationship between the excitation angle of BSWs and the position of the corresponding dark line on the prism can be calculated, as shown in Fig. S1. The dark line is the signature of the excitation of the BSWs mode. The geometric relationship satisfies $d/sin(pi/4-\vartheta) = x/sin(\vartheta)$. Here, d is the distance between the incident point (O) and the edge of the prism (O1), x is the distance between the dark line (O2) and the edge of the prism (O1). For different incident wavelength, the position of its dark line (O2) is changed (as shown in the right panel of Fig. S1a). As shown in Fig. S1b, this relationship is linear in a small angular range as $\vartheta = arctan(1/((d/x)^{0.5}-1))$, meaning that the position of the dark line is linearly related to the excitation angle of the BSWs. This dark line (or the reflected beam) was then imaged onto the camera, then the distance O1-O2 (x) was transformed to be x'' that can be defined by the number of the pixels along this line (the size of one pixel on the chip is a fixed value).

Using the transfer matrix method or numerical simulation, the curve of the excitation angle of the BSWs *vs*. the incident wavelength (that is the dispersion curve of the BSWs mode) can be calculated as shown in Fig. S1c. Then, based on Fig.S1b and Fig.S1c, the curve of the incident wavelength *vs.* x'' (number of the pixels) can be obtained as shown in Fig. S1d. As a result, the corresponding relationship between the incident wavelength and its position on the reflected image can be determined.

Based on the above descriptions, the procedures to measure an unknown spectrum can be illustrated as the workflow shown in Fig. S2.

Step 1, the dispersion curve is first calculated so that the relationship between wavelength and angle can be derived.

Step 2, when all the optical components of the experimental setup are fixed, there is a unique one-to-one relationship between the camera pixels and the angle of reflect light, which can be measured geometrically.

Step 3, the relationship between the incident wavelength and the position of its dark line on the image can be determined, and then the unknown spectrum can be reconstructed.

Here, the differential process is used to improve the accuracy of the spectra reconstruction.

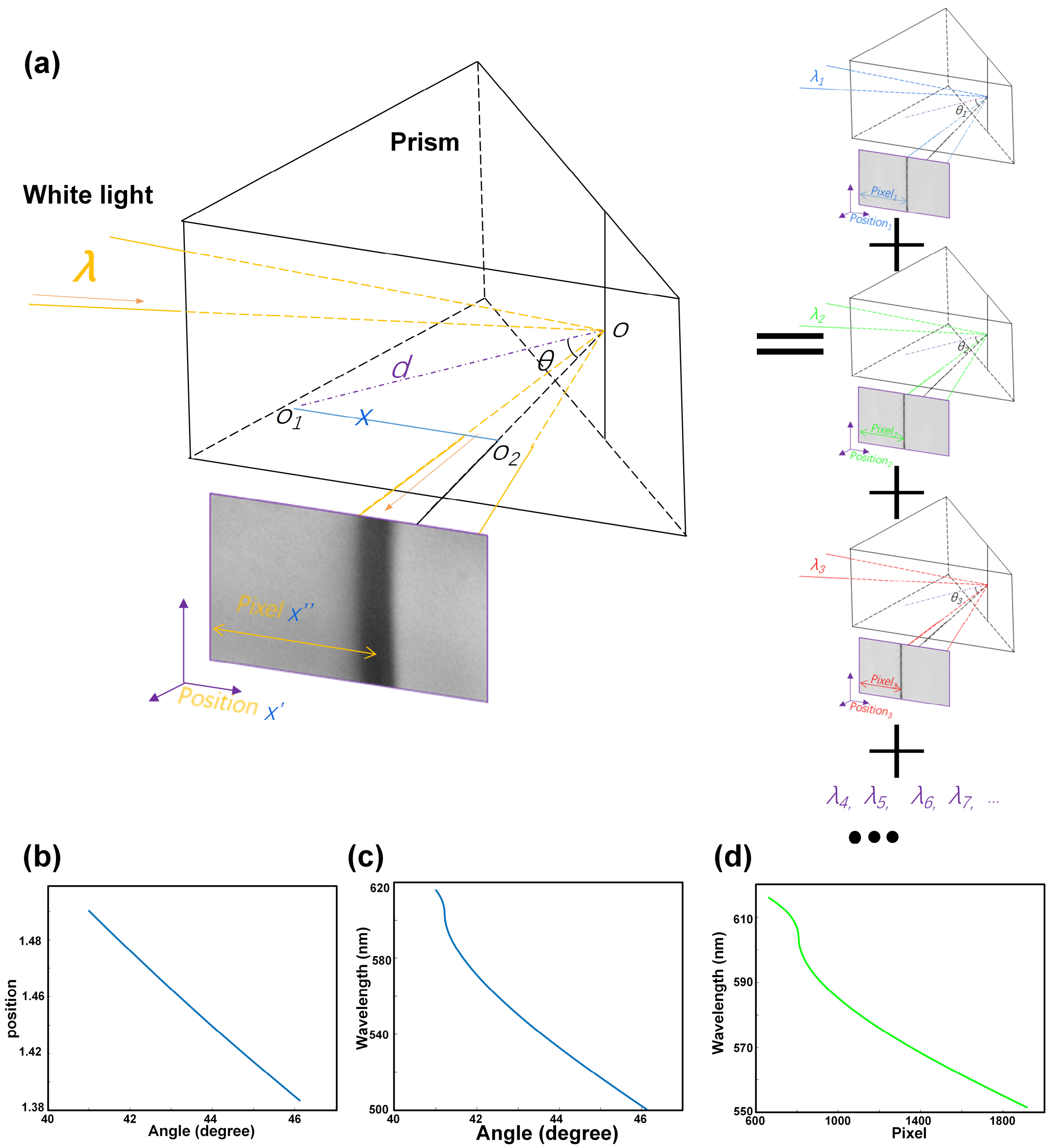

Figure S1 | The relationship between the wavelength of a light point and its spatial position on the reflectance image. (a) Schematic diagram to show the geometric relationship between the spatial position on the reflection image and the corresponding wavelength, when a broad band light is reflected from a prism. (b) According to the simple geometric relationship such as the size and position of the optical components in the actual optical path, the curve of the incident angles *vs.* the position on the reflected image was plotted. (c) The curve of the excitation angle of BSWs mode *vs.* incident wavelength was plotted based on numerical calculations. (d) The curve of the incident wavelength vs. the position (in the manner of pixels) on the reflected images was plotted based on the curves in (b) and (c), which will be used to reconstruct the spectrum from the reflection image.

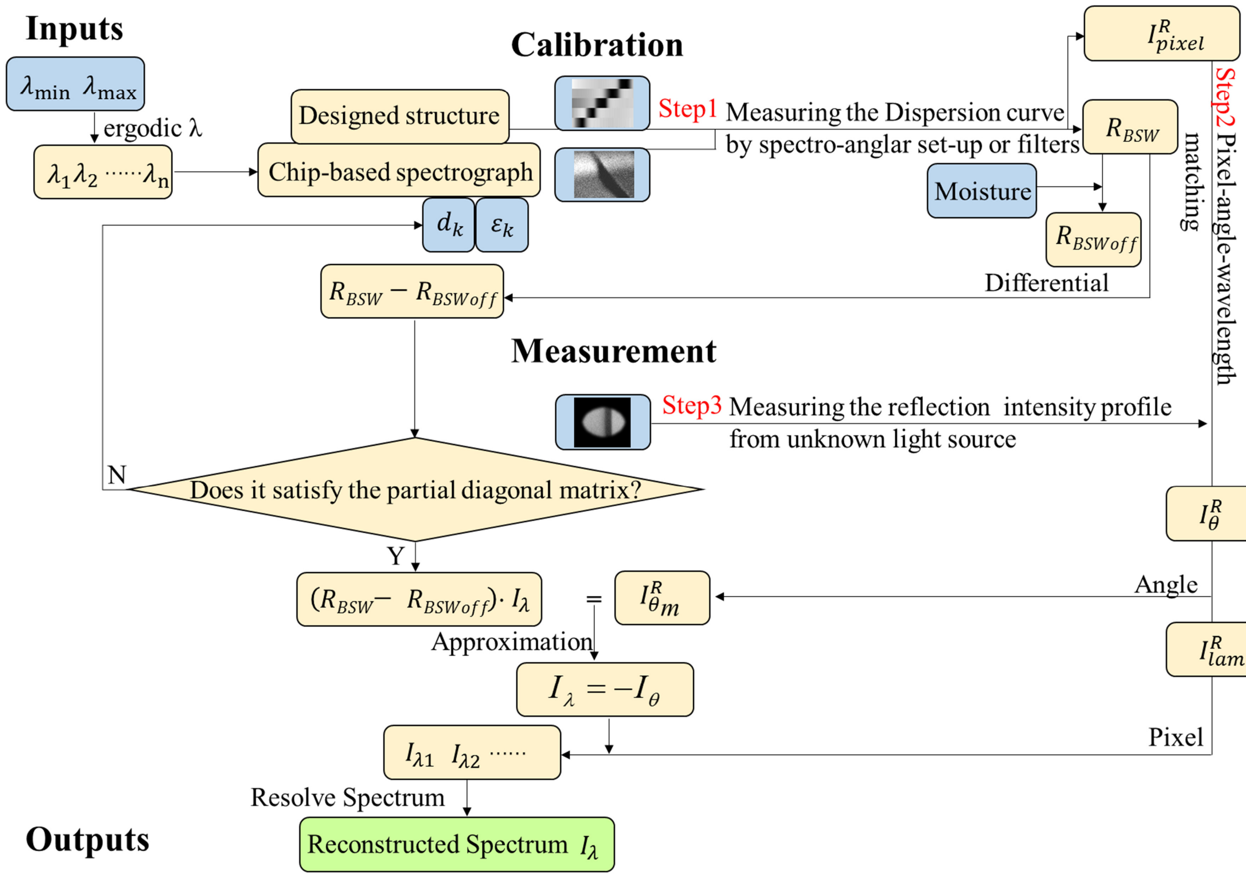

Figure S2 | The workflow of spectrum reconstruction. Blue blocks represent the measurement data and structural parameters, yellow blocks are processes and intermediate results, and the green block at bottom is the resolving spectrum.

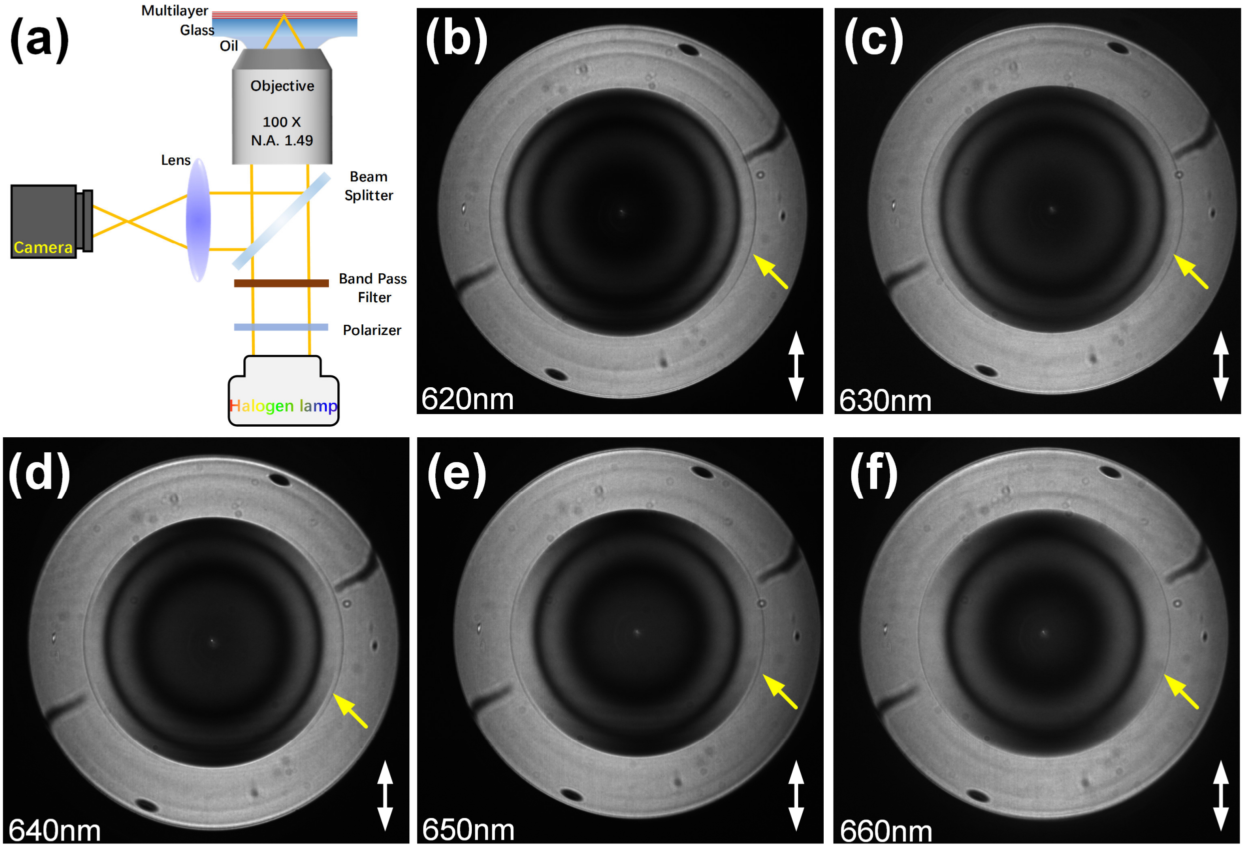

Figure S3 | Characterization of the dielectric multilayer with an LRM to determine the dispersion relation of BSWs mode. (a) The experimental setup of the LRM for BFP imaging the dielectric multilayer. BFP images of the dielectric multilayer with the incident wavelengths at (b) 620 nm, (c) 630 nm, (d) 640 nm, (e) 650 nm and (f) 660 nm.

In the experiment, the dispersion curves of the BSWs are characterized or calibrated with a home built leaky radiation microscope (LRM) as shown in Fig. S3a. Here, an oil immersed objective (CFI Apo TIRF ×100, numerical aperture NA = 1.49) from Nikon, Japan) was used for the back focal plane (BFP) imaging that can give out the angular dependent reflectance from the dielectric multilayer[4, 5]. The measured BFP images at discrete wavelengths are shown in Fig. S3b-S3f. The double arrow-headed lines represent the polarization orientation of the incident beam. The appearance of a pair of dark arcs on the BFP images verify the excitation of the transverse-electric (TE) polarized BSWs on the dielectric multilayer. From the known NA of the objective and the diameter of the dark arcs, the excitation angle of the BSWs at the corresponding incident wavelength can be derived [6, 7], then the dispersion curve of the BSWs is obtained.

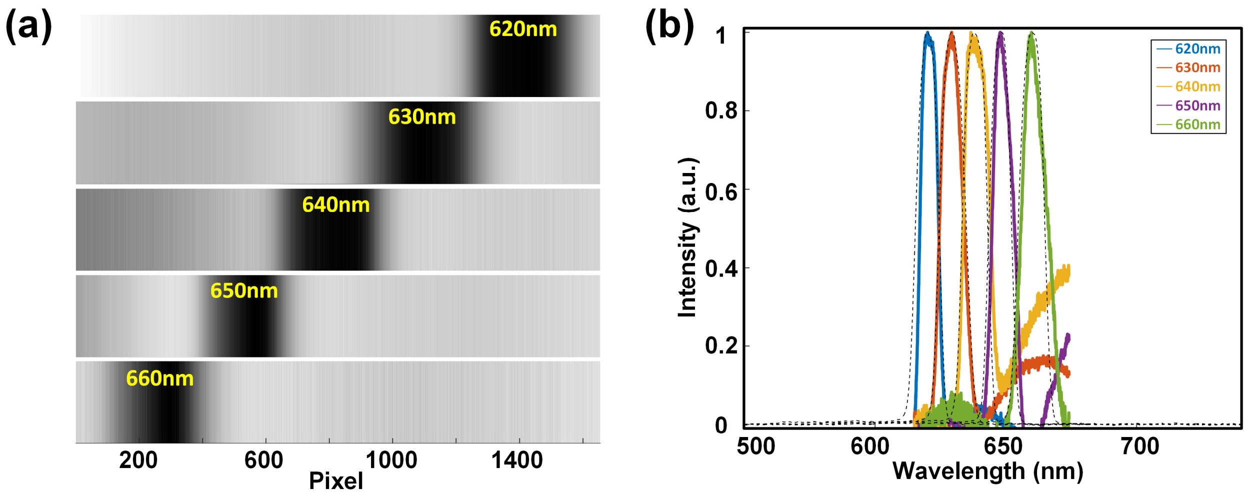

Figure S4 | Wavelength calibration of the chip-based spectrograph with a serial of band pass filters. (a) The spatial distribution of dark bands on the reflected image of a white light source, where a serial of band pass filters with different center wavelengths were used to filter the light source. The dark regions on the images are the signature of the excitation of BSWs at these wavelengths. (b) The spectra (solid lines) of the white light source (included a serial of bandpass filters) resolved from the chip-based spectrograph. The black dashed lines are the spectra measured with a commercial fiber optic spectrometer.

In our experiment, we also use another method to derive the corresponding relation between the incident wavelength (λ) and its pixel's position (x'') on the reflectance image. The experimental setup is the same as that used in Fig. 3e, where a serial of band pass filters with known center wavelengths are used to filter the broad band light source (Halogen lamp). Here, due to the used of these filters, the incident wavelengths' peaks are known. The light beam exiting from the halogen lamp passes through collimator with a series of alternative filters and then strike onto the prism. For each bandpass filter, two reflected images are captured, one is in the case that BSWs are excited, and the other is the case that the BSWs are not excited. The differential images are shown in Fig. S4a. Due to the use of the band pass filter, the excitation angle of the BSWs is confined to a small pixel area (the dark areas on the images) and gets narrower as the incident wavelength is red-shifted, which is in perfect agreement with the dispersion relationship in Fig. 1.

The band spectra are consequently detected and retrieved as the colored curves shown in Fig. S4b, which is consistent with the results (black dashed curves) measured by a fiber optic spectrometer (Ocean Insight, FLAME-T-VIS-NIR). As a result, the relationship between the incident wavelength (λ) and its pixel's position (x'') on the reflectance image can be easily calibrated from the known peak transmission wavelength of the band pass filter.

Note 3. Comparisons with conventional dispersive optics

Compared with the dark band formed by the dielectric multilayer attached prism under the illumination of white light source. Different colors are separated very well in Fig 3e and Fig. S4, meaning a high spectral resolution. The dispersion capability of the prism without the dielectric multilayer is shown in Fig. S5a, where broadband light sources are still almost spatially coincident, meaning a worse spectra resolution. The grating (1200 Lines Blazed at 500nm) with the similar parameters of the fiber optic spectrometer is also used as a comparison, where different wavelengths are separated far more than a prism, shown in Fig. S5b. However, a considerable portion of the light still overlaps. Both Fig.S5b and S5c demonstrate that in the absence of a slit, the spectra resolution of the conventional grating and prism is low.

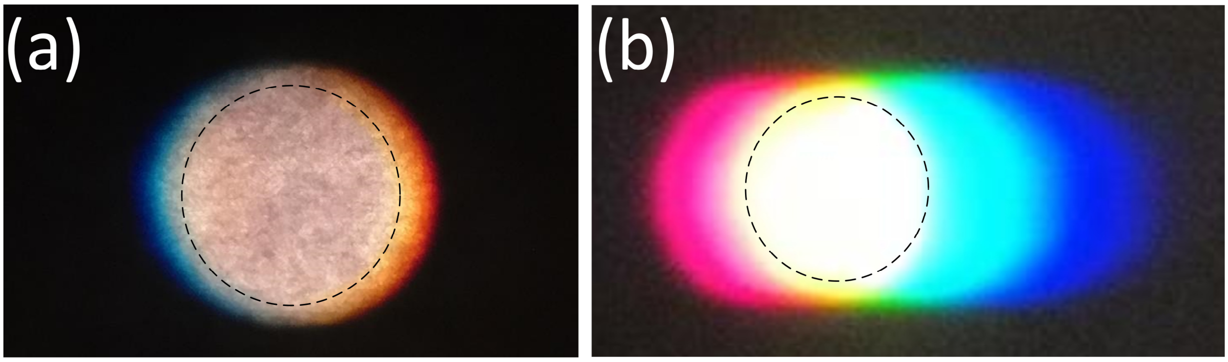

Figure S5 | Comparison of dispersion ability of different dispersive elements. (a) Dispersion capability of the prisms. The prism cannot spatially split the white light in color with high spectra resolution. Since there is no slit, the light of different wavelengths is overlapping, and the black dotted line indicates the size of the white light spot. (b) Dispersion capability of gratings. The grating can spatially disperse the white light, which is better than the prism. However, since there are no slits, there are still many wavelength bands of light that are overlapped, meaning the low spectra resolution.

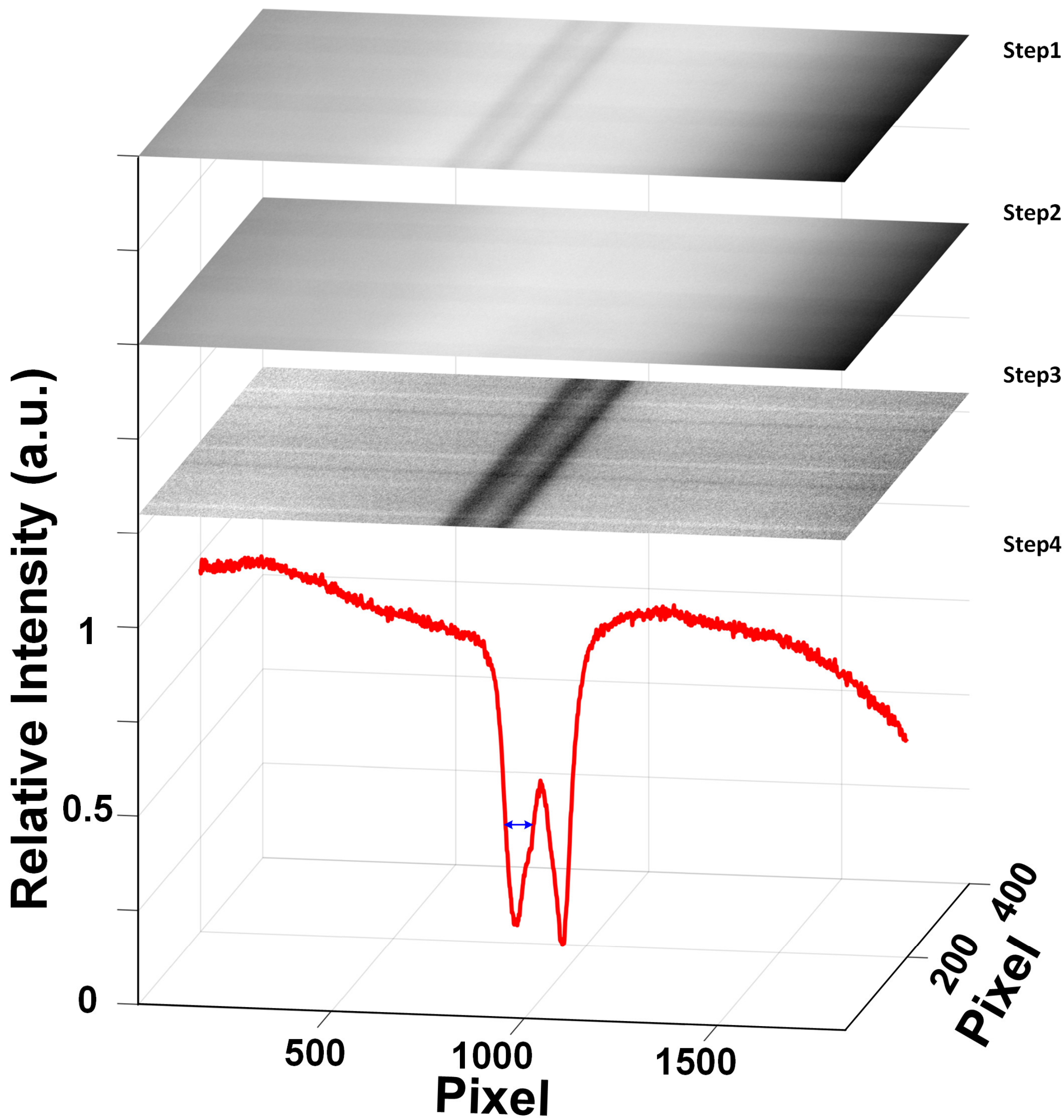

Figure S6| Verifying the spectral resolution of the chip-based spectrograph. Step1, the reflected image was captured in the case that the BSWs were excited on the dielectric multilayer. Step 2, the reflected image was captured in the case that the BSWs were not excited on the dielectric multilayer. Step 3, the differential image was obtained from the two images. Step 4, the profile along the horizontal direction of the differential image is plotted Two dark lines are distinct on the differential image and two valleys appear on the line-profile, meaning that the two wavelengths (589.0 nm and

589.6 nm) of the light emitting from the sodium lamp are resolved.

Note 4. The spectra response range of the dielectric multilayer based spectrograph

The spectral response range of the dielectric multilayer chip-based spectrograph can be adjusted through changing the structural parameters of the dielectric multilayer, as shown in Fig.S7. The corresponding relevant parameters for each of the data sets are shown in Fig. S7. The range with high reflection intensity consistency and high angular resolution of BSW coupling angle was selected during the optimization process. All commonly used wavelengths (from 169nm to 1041nm) from UV to NIR can be covered here, and their ranges can be adjusted to be larger if their spectral resolution is not strictly limited. The coupling angle of the BSWs and its angular coupling range can be obtained from the reflectivity curve. The central wavelength here represents the center of the operating wavelength range of the dielectric multilayer, which gradually redshifts as the thickness of the multilayer structure increases. In the short wavelength band, the spectral response is only about 70 nm, while an optimized dielectric multilayer can have a spectral response range of about 340 nm in the long wavelength band.

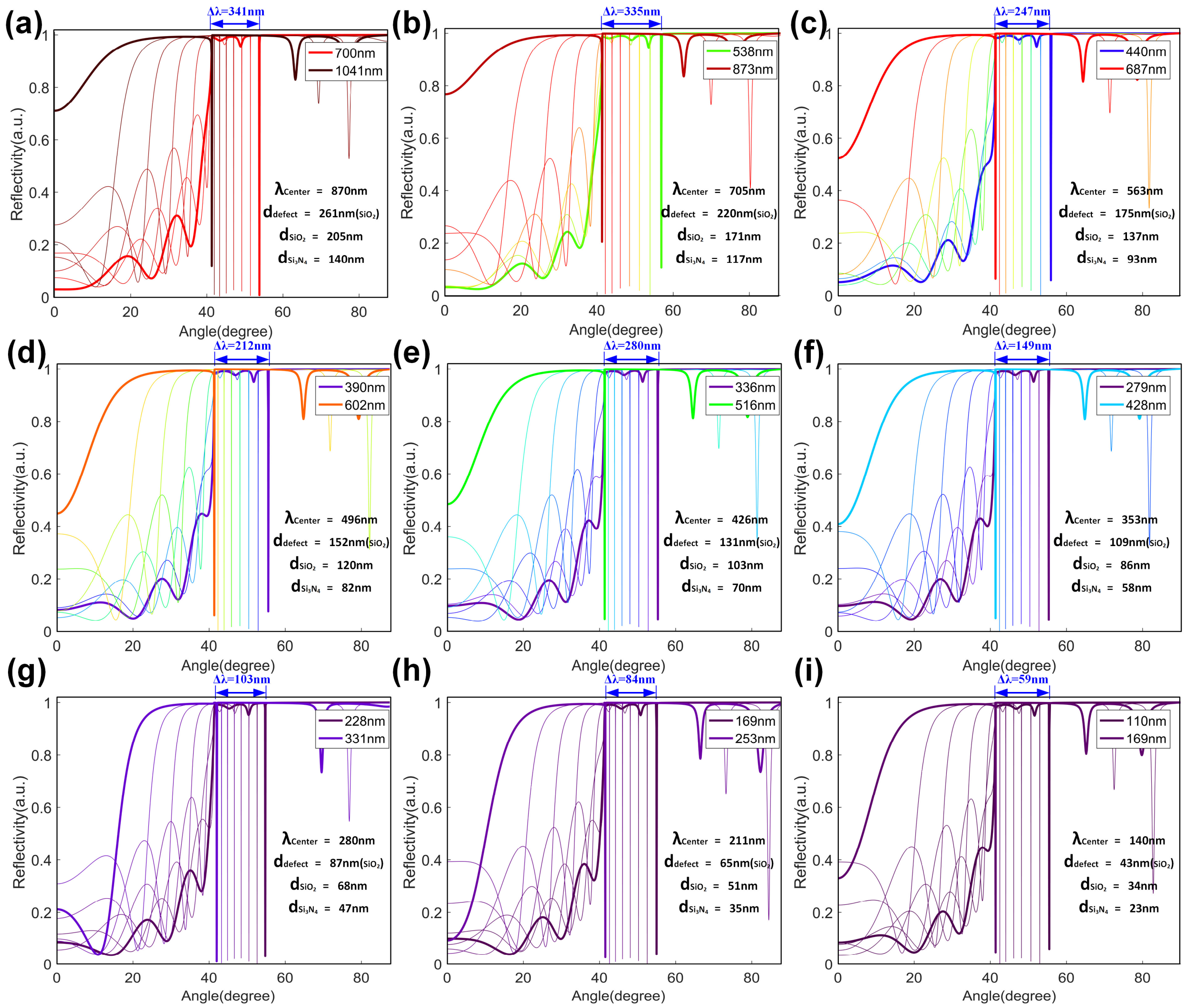

Figure S7 | Tuning the spectra response range of the dielectric multilayer structures. (a) – (i) Reflectivity curves for different structural parameters, showing the angular range over which the BSWs mode can be excited.

Note 5. Raman scattering signal acquired with the chip-based spectrometer.

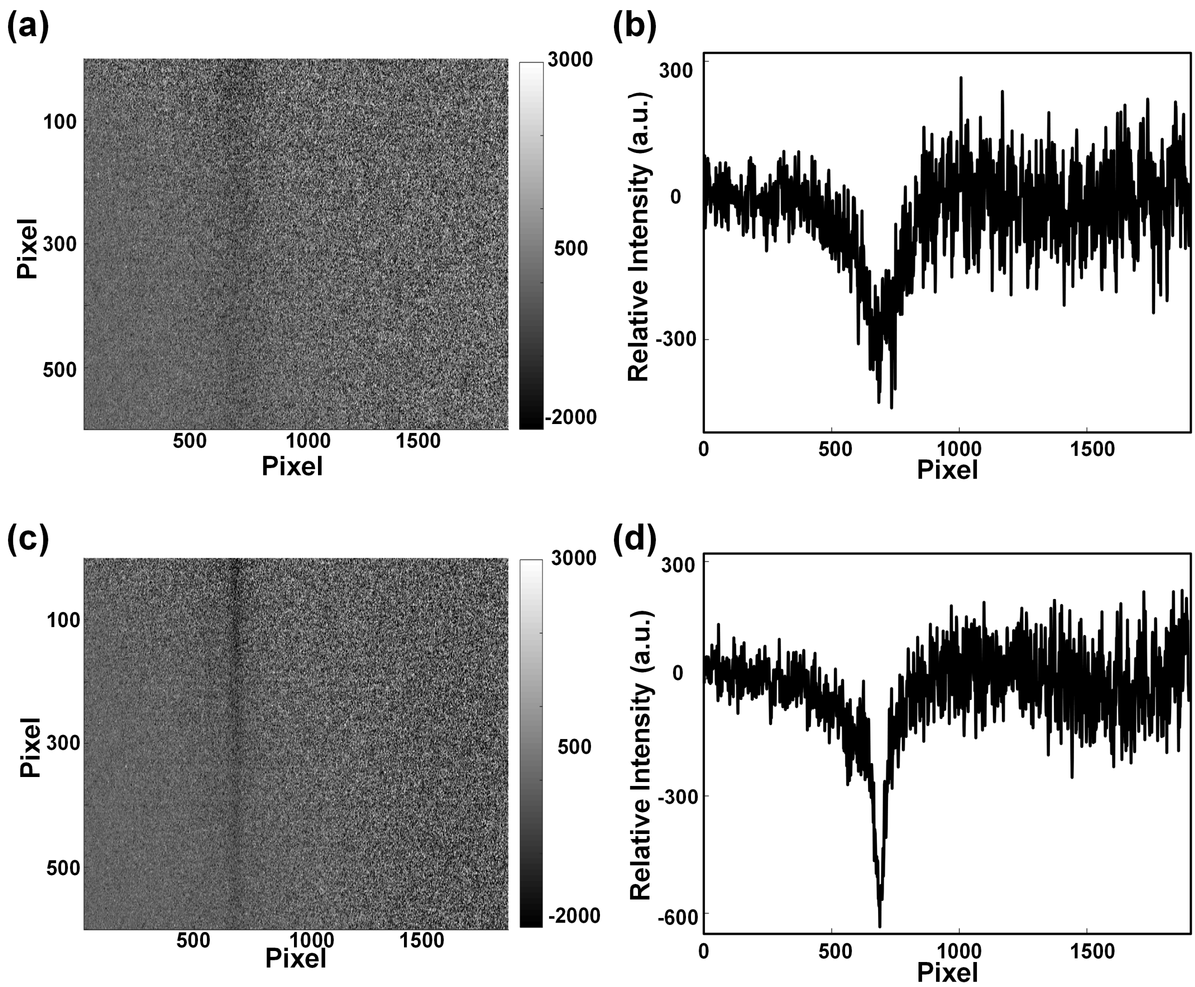

Figure S8 | Raman scattering signal captured by the camera of the chip-based spectrograph. The reflectance images captured by the camera when the samples are (a) ethanol solution and (c) DMSO solution. (b) and (d) are the intensity profiles along the horizontal direction of the images on (a) and (c), respectively.

The Raman scattering signal from different chemical bond vibrations with Raman shift can be reflected on different pixel positions of the camera. The wavelength of the Raman scattering signal is obtained based on the relationship between the pixel and the wavelength, which can be expressed as λ_m . Then, since the excitation light wavelength is known, the magnitude of Raman scattering spectrum shift can be calculated by,

$$RamanShift = 1/\lambda_0 - 1/\lambda_m \quad \text{(S12)}$$

Here, λ_0 is the wavelength of the laser beam, which is 532 nm. λ_m is the wavelength of the Raman scattering light.

References

1. Chen YK, Shen ZH. Near-field spectrum retrieving through non-degenerate coupling emission. *Nanophotonics* 2020, **9**(1)**:** 235-243.

2. Yang Z, Albrow-Owen T, Cui H, Alexander-Webber J, Gu F, Wang X*, et al.* Single-nanowire spectrometers. *Science* 2019, **365**(6457)**:** 1017-1020.

3. Wang R, Lei X, Liu L, Wu L, Wu A. Bloch Surface Waves Mediated Micro‐Spectroscopy. *Small* 2021, **17**(49)**:** 2103688.

4. Kuai Y, Xie Z, Chen J, Gui H, Xu L, Kuang C*, et al.* Real-Time Measurement of the Hygroscopic Growth Dynamics of Single Aerosol Nanoparticles with Bloch Surface Wave Microscopy. *Acs Nano* 2020, **14**(7)**:** 9136-9144.

5. Fan Z, Kuai Y, Tang X, Zhang Y, Zhang D. Chip-based wide field-of-view total internal reflection fluorescence microscopy. *Opt Lett* 2022, **47**(17)**:** 4303.

6. Kuai Y, Chen J, Fan Z, Zou G, Lakowicz JR, Zhang D. Planar photonic chips with tailored angular transmission for high-contrast-imaging devices. *Nat Commun* 2021, **12**(1).

7. Kuai Y, Chen JX, Tang X, Xiang YF, Lu FY, Kuang CF*, et al.* Label-free surface-sensitive photonic microscopy with high spatial resolution using azimuthal rotation illumination. *Science Advances* 2019, **5**(3).